Progress In Electromagnetics Research C, Vol. 139, 45–57, 2024

A Combinatorial Approach to Quantitative Microwave Imaging for Breast Tumour Profiling Using SVBIM and SpaRSA

Ria Benny*, Thathamkulam A. Anjit, Philip Cherian, and Palayyan Mythili

Abstract—A combinatorial quantitative reconstruction method employing Subspace-based Virtual Born Iteration Method (SVBIM) along with a greedy compressive sensing algorithm, Sparse Reconstruction by Separable Approximation (SpaRSA) to solve the ill-posed inverse problem in microwave imaging is proposed in this paper. SVBIM makes use of the contribution of the variational induced current to arrive at a better estimate of the permittivity profile in each iteration. SpaRSA operates in the sparse domain and reduces the computational overload, thereby guiding the inverse problem towards a faster global optimum solution. The merger of these two algorithms helps to reconstruct breast profiles having high-permittivity tumor inclusions ($\varepsilon = 60$) with reduced error. The proposed reconstruction method is capable of extracting the salient information regarding tissue differentiation (permittivity and conductivity) and dielectric distribution of various tumor and fibroglandular inclusions, dimensions, resolution, size, shape, and coordinate localization of inclusions. In comparison to various methods reported in literature, the results obtained using the proposed method are highly encouraging. In the presence of 30 dB noise, the above-said imaging technique produces a significantly reduced permittivity error value of 0.47 in the reconstruction of tumor inclusions as against 0.85 and 0.71 in the case of TV norm and Re-weighted Basis Pursuit methods, respectively. The experimental validation is carried out using a phantom having three inclusions of sizes 10 mm, 6 mm, and 3 mm. The inclusions have been localized successfully with errors of 0.089, 0.133, and 0.21, respectively.

1. INTRODUCTION

Microwave imaging (MWI) is a technique used for estimating the properties of an object by processing the signals scattered off the object. Since it is a safe, non-ionizing and affordable imaging modality, it is highly suitable for biomedical applications like breast tumor detection. MWI is based on the dissimilarity in dielectric properties of malignant and normal tissues at microwave frequencies [1, 2]. MWI can proceed through qualitative or quantitative techniques. Qualitative imaging methods can determine the contour and position of the object under study and are useful for detecting the presence of inhomogeneities. The quantitative methods can additionally develop the permittivity profile of the scatterer by solving the Inverse Scattering Problem (ISP) leading to the differentiation of the tumor and fibroglandular tissues present amongst the normal fatty breast tissues. Although majority of the breast volume is composed of fatty adipose tissues having high dielectric contrasts as compared to malignant cells, tumors usually sprout out from regions in and around the fibroglandular connective tissues commonly possessing low variation in permittivity to fatty tissues. Therefore, the correct differentiation of these tissues is needed to locate the actual spread of tumors to aid further invasive treatment procedures.

The ISP which has to be solved to obtain a permittivity profile of the constituting tissue types is highly ill-posed and nonlinear in nature. Reconstruction of the dielectric profile from the ISP is

Received 4 July 2023, Accepted 28 October 2023, Scheduled 2 December 2023
* Corresponding author: Ria Benny (riabenny2802@gmail.com).
The authors are with the Cochin University of Science and Technology, Cochin, Kerala, India.

achieved by solving the Electric Field Integral Equations (EFIE). These integral equations are nonlinear in nature because two sets of unknown quantities (the dielectric profile and the total electric field inside the scattering object) have to be solved for, simultaneously [3].

The solution to the ISP can be iteratively obtained through stochastic or deterministic methods. Stochastic methods are powerful tools as they can converge to a global minima [4]. However, due to the computational complexity involved deterministic methods are preferred more. Deterministic methods, which include Newton type and gradient based methods, are, however, inefficient in converging to an optimum solution due to the large degree of nonlinearity involved in the ISP [5, 6]. Hence, they are often supported by various regularization and optimization techniques. Regularization schemes solve the ISP by replacing the original ill-posed problem by a well-posed one by incorporating some additional information (a-priori information) [7]. Sampling-based reconstruction [8] involving properly designed imaging functionals was adopted in [9] to recover anomalies buried in a two-layered medium. The commonly used regularization methods like Tikhonov method, total variation, etc. employ the l_2-norm minimization [10]. The problem with the use of l_2-norm is that it produces extra smoothness and becomes drastically inefficient when being applied to domains with sharp variations, discontinuities, or sparse content. Therefore, the sharpness provided by l_1-norm was adopted by researchers instead of l_2-norm [11]. The l_1-norm-based implementation received a huge support with the advent of Compressive Sensing (CS).

Compressive Sensing pioneered by Candès and Wakin [12] is an approach for reconstructing a signal even when it has been sampled significantly below the Nyquist rate. CS techniques operate in the sparse domain and are capable of providing accurate reconstruction results even when the dimensionality of the measurement data is much less than the number of unknowns in the inverse problem. Such sparsity-promoting regularized approaches in CS domain express the unknown functions as a sparse set of coefficients with respect to an appropriate basis [13]. Total Variation CS method [14] proposed by Li and Osher proceeds by minimizing the integral of the gradient of the contrast function. However, this method produced low convergence rates while dealing with a large number of degrees of freedom. Bayesian techniques using probabilistic modeling was another promising optimization technique as they involved small number of control parameters and could provide accurate reconstruction [15]. However, the method proved to be computationally intensive for implementation.

Numerical studies that attempt to solve the ISP by employing limited-aperture data was extensively taken up by Liu et al. [16, 17]. Minimum number of far field measurements are used in providing the reconstruction of inhomogeneities accurately. These scenarios involving highly nonlinear and ill-posed inverse problem are practically important and highly challenging due to the severe lack of information [18]. Neural network based solvers employing Long Short-Term Memory (LSTM) neural network, Fully Connected Neural network (FCNN), etc. have helped to break through the resolution limit imposed by limited-aperture data [19, 20]. A recent area of research in the ISP domain involves the non-iterative techniques based on deep learning [21–23]. These learning-based methods have the capability of producing reconstruction results within seconds and can be implemented for real-time imaging. However, with the existing computational resources, the permittivity range reported by such methods is low (up to $\varepsilon = 10$) [24, 25]. Therefore, the non-iterative solvers are unsuitable for medical imaging or tumor detection applications because actual tumor tissues in humans have permittivity values ranging around $\varepsilon = 60$ [26]. The iterative methods, on the other hand, are seen to reconstruct higher values of permittivity, although the reconstruction of permittivities in the range of 60 has been reported only by a few researchers. This is because solving for higher values of dielectric constant in the EFIE equations leads to greatly ill-posed and complex ISP scenarios, and under such situations, most of the iterative algorithms tend to diverge away from the solution. Hence, it may be observed that robust iterative imaging techniques capable of converging to an optimum solution while reconstructing breast profiles having high-ε tumor inclusions with reduced error are needed in the field of MWI.

In this paper, an iterative solver that combines SVBIM algorithm with SpaRSA is implemented to solve the ISP for breast tumour profiling. SVBIM is an improved version of DBIM (Distorted Born Iterative Method) wherein the total electric field is estimated by adding the contribution of the induced current, which makes it more accurate than the Born approximation used in most iterative solvers [27]. It may be noted that SpaRSA is a very robust CS algorithm that proceeds with an adaptive thresholding methodology to find a global minimum solution. This makes the combinatorial

technique discussed in this work adept in solving a highly ill-posed ISP involving high permittivity tumor growths. The method is observed to reconstruct breast profiles with single or multiple inclusions of tumours/fibroglandular tissues with reduced error values as compared to [3] and [7]. Additionally, the performance of the proposed iterative method has been validated by reconstructing available experimental data and comparing it with the results reported in [3] and [5].

The paper is structured in the following manner. Section 2 discusses the imaging scenario and how the permittivity profile of the object is reconstructed by the proposed method that combines SVBIM and SpaRSA. In Section 3, the simulation and experimental study are described in detail, and the results obtained are compared with literature. Finally, the paper conclusion is provided in Section 4.

2. PROBLEM STATEMENT

In this section, the deterministic reconstruction method proposed in this paper with an aim to reconstruct the permittivity profile of the object under study is described in detail. The scattered field data measured at the antennas is used by the imaging algorithm to solve the ISP. Section 2.1 explains the imaging process in MWI and introduces the concepts of forward problem and inverse problem. In Section 2.2, the reconstruction algorithm, namely, Subspace-based Virtual Born Iteration Method is explained. The compressive sensing-based SpaRSA method used for solving the ISP is elaborated in Section 2.3.

2.1. Imaging Scenario in MWI

The tomographic imaging process in MWI is completed by solving the forward scattering problem and inverse scattering problem. The forward scattering process begins by illuminating the object under study using microwave signals from antenna sources (transmitters). The object acts as an inhomogeneity in the path of the waves. So, scattering of these waves occurs in all directions and they are in turn collected at the receiver antennas arranged around the object. From the collected data, an estimate of the spatial distribution of the dielectric properties (permittivity and conductivity) of the scatterer is obtained by solving the ISP.

Figure 1 shows the schematic arrangement of the transmitter antennas (N numbers) and receiver antennas (M numbers) for the collection of the scattered data. The antennas are assumed to illuminate the object under study with waves having TM polarization. The dielectric constant, ε_r, within the object is inhomogeneously distributed.

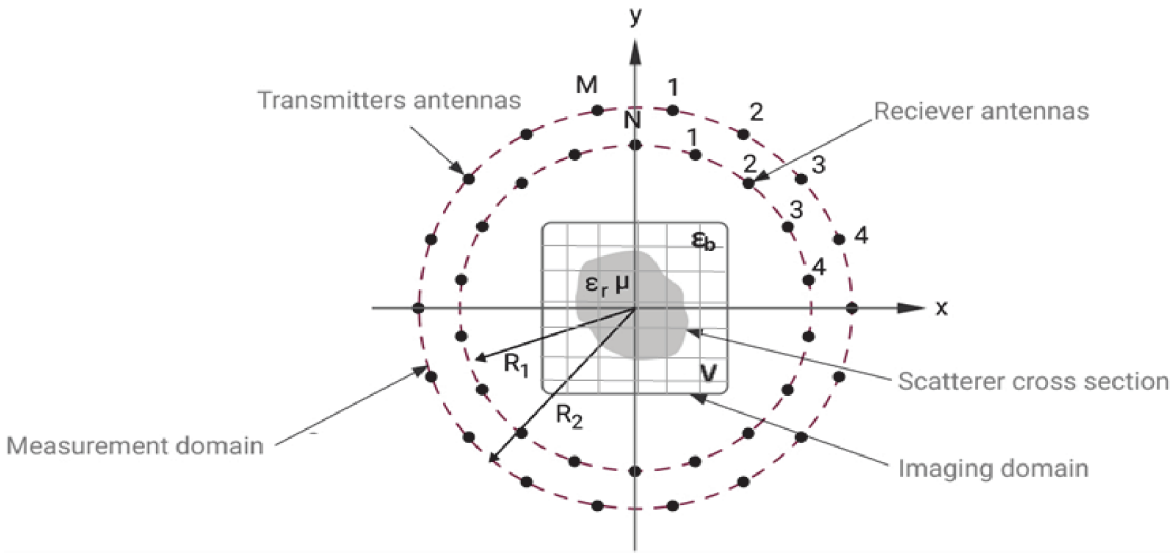

Figure 1. Schematic diagram showing the antennas positioned around the object under study.

The background medium surrounding the object is assumed to be homogeneous in nature with a constant permittivity of ε_b. Since a 2D scattering problem is considered in this paper, the dielectric profile variations are limited to a single plane (X-Y plane in this case). The expression for the complex dielectric constant is given by

$$\varepsilon = \varepsilon' + j\frac{\sigma}{\omega} \tag{1}$$

Here, the real part, ε', represents the permittivity, and σ in the imaginary part represents the conductivity. The region, V around the object for which permittivity reconstruction is done, is called the object domain or imaging domain. The region comprising the antennas where the measurements are collected is called the measurement domain. The transmitter/receiver antennas are usually positioned on a circle of radius R_1 and R_2, respectively.

In microwave imaging process, the first step (forward problem) involves the transmitting antennas illuminating the object from multiple angles. The receiver antennas will then collect the signals scattered off the object. Method of Moments (MoM) can be used to solve the forward problem.

The total electric field, $E_{tot}(r)$, at any point r is the sum total of the incident filed, $E_{inc}(r)$, transmitted from the antennas (in the absence of object) and the scattered waves, $E_{scat}(r)$, which are bounced off the object.

$$E_{tot}(r) = E_{inc}(r) + E_{scat}(r) \tag{2}$$

Integral equations called the Electric Field Integral Equation (EFIE) can be used to formulate the total field in the area, V. It is a set of two equations namely the state equation and data equation. According to the State equation, the total field, $E_{tot}(r)$, is given by:

$$E_{tot}(r) = E_{inc}(r) + \int_V g(k_0; r, r')[k^2(r') - k_0^2(r')]E_{tot}(r')dr' \tag{3}$$

Here, $g(r)$ is the Green's function, and k_0 is the wave-number of the background medium. $k(r)$ is the varying value of the wave-number for each point in the region, V. Equation (3) is said to be ill-posed because the total field term appears on both sides of the integral equation. When being discretized, Equation (3) is given by:

$$E_{tot} = E_{inc} + G_V \cdot \varepsilon \cdot E_{tot} \tag{4}$$

where ε represents the complex permittivity distribution matrix, and G_V is the object Green's function. Rewriting Equation (3) we get:

$$E_{tot} = (I - G_V \cdot \varepsilon)^{-1} \cdot E_{inc} \tag{5}$$

Here, I is the identity matrix. The Data Equation gives the expression for the scattered field received at the antennas positioned around the scatterer in the measurement domain which is given by:

$$E_{scat} = G_s \cdot \varepsilon \cdot E_{tot} \tag{6}$$

where G_s is the measurement Greens function. The data equation and state equation can be combined to form the following final expression for the calculation of the scattered field data in the forward problem:

$$E_{scat} = G_s \cdot \varepsilon \cdot (I - G_V \cdot \varepsilon)^{-1} \cdot E_{inc} \tag{7}$$

With the knowledge of the scattered fields from Equation 7, solving for the contrast function and thereby the dielectric profile of the scatterer can be carried out. This is termed as the inverse problem or ISP. However, since this inverse problem is highly nonlinear, an exact solution cannot be determined accurately. Hence, various approximations are necessary to linearize the EFIE equations and solve the inverse problem. Section 2.2 elaborates the linearization of the ill-posed EFIE equations using the SVBIM method, and Section 2.3 explains the optimization process using CS technique.

2.2. Iterative Solution to the Inverse Problem Using SVBIM

The inverse problem consists of reconstructing the spatial distribution of the dielectric contrast function in the imaging domain, V using the finite measured scattered field data available at the receivers. Various approximations can be used to linearize the ill-posed and non-linear EFIE equations like Born approximation, Rytov approximation, etc. Following the linearization, an iterative procedure (like

BIM, DBIM, Variational BIM (VBIM), SVBIM etc.) may be applied to progressively arrive at the best solution. The SVBIM solver used in this work updates the Green's function for the inhomogeneous background at each iteration, and then by performing the Singular Value Decomposition (SVD) on the radiation operator matrix, it retrieves the deterministic subspace of the induced current. Therefore, the total electric field can be estimated by adding the contribution of the induced current, which is more accurate than the Born approximation in BIM or DBIM.

In both VBIM and SVBIM, the variational form of the scattered field expression of Equation 7 is used in the iterative procedure. Hence, at the kth iteration:

$$\delta E_{scat} = G_s \cdot \delta\varepsilon_k \cdot (I - G_V \cdot \varepsilon_{k-1})^{-1} \cdot E_{inc} \tag{8}$$

where δE_{scat} corresponds to the variation in value of scattered field calculated in the kth iteration using the algorithm and the corresponding measured value. The $\delta\varepsilon$ in the equation is the permittivity value variation in kth and $(k-1)$th iterations. The EFIE can be expressed in terms of the induced current, as:

$$E_{tot} = E_{inc} + G_V \cdot J \tag{9}$$

where J is the induced current which is not readily available. VBIM technique approximates J using J_{k-1} generated by ε_{k-1}. On the other hand, SVBIM uses $(J_{k-1} + \delta J^d)$ to obtain the induced current value. If δJ^d is the deterministic part of the variational induced current (δJ),

$$E_{tot} = E_{inc} + G_V \cdot \left(J_{k-1} + \delta J^d\right) \tag{10}$$

If the iteration is convergent, then J_k produced by SVBIM is closer to the exact induced current, J, than J_{k-1}. Hence, SVBIM has a faster convergence speed than VBIM [27].

In Equation 10, the expression for the term (δJ^d) is given by:

$$\delta J^d = \sum_{i=1}^{L} \frac{u_i^* \cdot \delta E_{scat}}{\sigma_i} \tag{11}$$

In the above equation, the terms u_i, v_i^*, and σ_i are obtained by the Singular Value Decomposition (SVD) of the mapping function, G_s. The application of SVD gives $G_s = \sum_i u_i \sigma_i v_i^*$ and $G_s \cdot v_i = \sigma_i u_i$. When singular value representation is used for δE^{scat} noise easily affects those singular values with less magnitude. So, the singular values are first sorted in the order of reducing amplitude, and then only the significant 'L' values are used. In SVBIM, the integer value can be selected for 'L' (in this work $L = 15$) which is simpler than Tikhonov method where the regularization parameter can vary in the entire range of real numbers.

The cost function for the SVBIM is defined as a sum of the mismatch of the variational scattering field normalized by the measured scattered field, and the variational induced current inside the imaging domain normalized by the deterministic part of the variational induced current, given by:

$$f(\delta\zeta) = \frac{\|\delta E^{scat} - G_s \cdot \delta\zeta \cdot E^{tot}\|^2}{\|E^{scat}\|^2} + \frac{\|\delta\zeta \cdot E^{tot}\|}{\|\delta J^d\|^2} \tag{12}$$

This cost function is minimised iteratively to solve the ISP. However, the ill-posedness of the ISP may offer issues in convergence. Hence, in this paper, compressive sensing is combined with SVBIM, which is discussed in Section 2.3.

2.3. Solution to the Inverse Problem under the Compressive Sensing Framework

In MWI, iterative solvers like SVBIM alternate between the forward and inverse problems to estimate the permittivity profile. However, the constraints on the number of unknowns to be estimated from a set of under-determined EFIE equations makes it a challenging problem. To overcome this hurdle, the solution to the ISP is determined by employing the SVBIM method under the Compressive Sensing (CS) framework. CS is a methodology for signal reconstruction from a measurement vector which is smaller in size than the Nyquist-sampled signal vector. CS has the potential to recover a high-dimensional signal exactly or accurately from smaller number of measurements. Hence, it is a very useful tool in the case of MWI where the amount of scattered data available for reconstruction is very limited.

To solve for the object profile, the SVBIM technique approximates the ill-posed inverse problem as a linear problem given by $\mathbf{y} = \mathbf{A} \cdot \mathbf{x}$. Here, the scattered fields are represented by the matrix on the left hand side, $\mathbf{y}$ of size $(M \times 1)$. The matrix $\mathbf{A}$ is the product of the Greens function and total field, which is also a known quantity. The only unknown to be solved for is the permittivity distribution, $\mathbf{x}$ (size $(P \times 1)$). The number of measurement points, M, is always very much lesser than the resolution of the image, i.e., $M \ll P$. Therefore, the problem to solve for the contrast profile is always ill-posed.

To solve the ill-posedness, the sparsity of the vector $\mathbf{x}$ is exploited under the CS framework. A relatively small number of random projections of a sparse signal can contain most of its salient information. Hence, by applying CS methods, the reconstruction of the dielectric profile from the ISP involving large number of unknowns is made possible starting from the limited set of measurement scattered data. Hence, the resolution of the image that can be produced with CS techniques from the available data is much higher than that reconstructed by conventional imaging algorithms.

In this paper, the CS method named Sparse Reconstruction by Separable Approximation, SpaRSA, is adopted. It is a powerful tool that combines the aspects of convex optimization, linear algebra, and dimensionality reduction to automatically determine near-optimal sparse approximations. It is known that many signals and systems can be represented as a linear combination of elementary mathematical functions. This CS method is adept in selecting a small number of such functions which is a subset of a large set of possible functions, so that the signal or system can be represented effectively as a linear combination of this subset. The algorithm proceeds by solving an l_1-l_2 optimization sub-problem [28] and is capable of finding sparse approximate solutions to even large under-determined linear equations. This method has the advantage of being capable of converging to a global minimum. It benefits from the use of a good approximate solution as a starting point. In the SpaRSA method, a sub-problem is set up and solved efficiently at each iteration, which is expressed as:

$$x^{t+1} \in \arg\min_{z} \ \frac{1}{2}\|z - u^t\|_2^2 + \frac{\tau}{\alpha_t} c(z) \tag{13}$$

where

$$u^t = x^t - \frac{1}{\alpha_t} \nabla f\left(x^t\right) \tag{14}$$

The above equations show that SpaRSA belongs to the class of Iterative Shrinkage and Threshold (IST) algorithms. SpaRSA is actually a kind of accelerated IST, with improved practical performance [29]. The algorithm shown below is followed to implement SpaRSA method in this work.

Algorithm 1 Reconstruction Algorithm

1: Choose factor $\eta > 1$, and constants $\alpha_{\min}$ and $\alpha_{\max}$ (with $0 < \alpha_{\min} < \alpha_{\max}$);
2: Initialize iteration counter, t←0; choose initial guess x^0;
3: Choose $\alpha_t \in [\alpha_{\min}, \alpha_{\max}]$;
4: $x^{t+1} \leftarrow$ solution of subproblem (12);
5: $\alpha_t \leftarrow \eta \alpha_t$;
6: **until** x^{t+1} satisfies acceptance criterion;
7: $t \leftarrow t + 1$;
8: **until** stopping criterion is satisfied.

At each iteration, the column that reduces the approximation error the most is selected. In the case of microwave imaging, $\mathbf{A}, \mathbf{x}$, and $\mathbf{y}$ are complex entities. Hence, in Equation 13, $c(z) = \|z\|_1$, and the unique minimizer is expressed as

$$\arg\min_{z \in C} \ \frac{|\, z - u^t \,|^2}{2} + \frac{\tau \,|\, z \,|}{\alpha_t} = soft\left(u_i^t, \frac{\tau}{\alpha_t}\right) \tag{15}$$

In this work, a combination of SVBIM and SpaRSA is employed to reconstruct the dielectric permittivity profile from the scattered data. Simulation and experimental studies are undertaken to evaluate the performance of the proposed method. The reconstruction results obtained upon solving the ISP are discussed in Section 3.

3. RESULTS AND ANALYSIS

In this work, the inverse scattering problem is solved using the combination of SVBIM and CS technique to profile various breast geometries. This section presents the results of the simulation study and experimental analysis. To assess the proposed method thoroughly, a quantitative analysis is necessary. For this purpose, Root Mean Square Error (RMSE) is calculated to compare the output image produced by the proposed method with the actual dielectric profile of the object under study using the following equation:

$$RMSE = \sqrt{\frac{1}{M}\sum_{i}\sum_{j}\left|\frac{\varepsilon^{r}_{r;i,i} - \varepsilon^{t}_{r;i,j}}{\varepsilon^{t}_{r;i,j}}\right|^{2}} \tag{16}$$

where $\varepsilon^{r}_{r;i,i}$ & $\varepsilon^{t}_{r;i,j}$ stands for the permittivity profile produced by the proposed method and the actual permittivity profile; ($i = 1, 2, \ldots, M_1$; $j = 1, 2, \ldots, M_2$; and the total number of pixels $M = M_1 \times M_2$.

3.1. Simulation Results

In the simulation study taken up in this section, a tomographic imaging setup is considered with antennas arranged at a radius of 12 cm around the breast model to be imaged. Here, the 32 transmitters (M) send out microwave signals in the 3–4 GHz range. These signals are scattered away by the breast phantom, and they are collected by the 32 receiver antennas (N). Hence, in this study, the scattered signals generated by the forward problem for a single frequency will be of size 32×32. The total dataset obtained for 20 frequencies is given as the input to the proposed method to generate the dielectric profile of the phantom.

In any practical imaging scenario, the scattered data collected will always be affected by the presence of various kinds of noises. To account for all the noise sources, the simulation study in this section is performed in the presence of an additive Gaussian noise of 30 dB. In such a realistic noisy environment, the performance of the proposed method is analyzed using a breast profile (profile 1) with multiple inclusions of tumor and fibro-glandular tissues. The dielectric values considered for different breast tissues in profile-1 are shown in Table 1.

Table 1. Dielectric constant for tissues in breast profile-1.

Tissue type [30, 31]	ε_r
Skin	32
Fatty breast tissue	9
Fibrous tissue	11
Tumors	60

In this numerical analysis, profile-1 used has two tumor inclusions of size 6 mm and two inclusions of fibro-glandular tissues of radius 10 mm implanted within the fatty breast tissues (as shown in Figure 2(a)). The breast phantom is of radius 50 mm, and a thin layer of skin of thickness 5 mm encloses the fatty breast tissues. The difference in dielectric constant between the normal and the malignant tissues is very large, resulting in a highly ill-posed scenario. On the other hand, the dielectric contrast between the normal fibro-glandular tissues and the fatty breast tissues is very small, thereby making the differentiation difficult. The reconstructed image obtained using the proposed method is shown in Figure 2(b).

From Figure 2(b), it can be seen that visualization of all inclusions is performed. Table 2 tabulates the RMSE values in the reconstruction of various kinds of tissues in profile-1. The table clearly shows that proposed SVBIM-SpaRSA method is capable of reconstructing the tumors with high permittivity values. Identification of the fibro-glandular tissues which have small variation in dielectric permittivity from normal fatty breast tissues is also achieved.

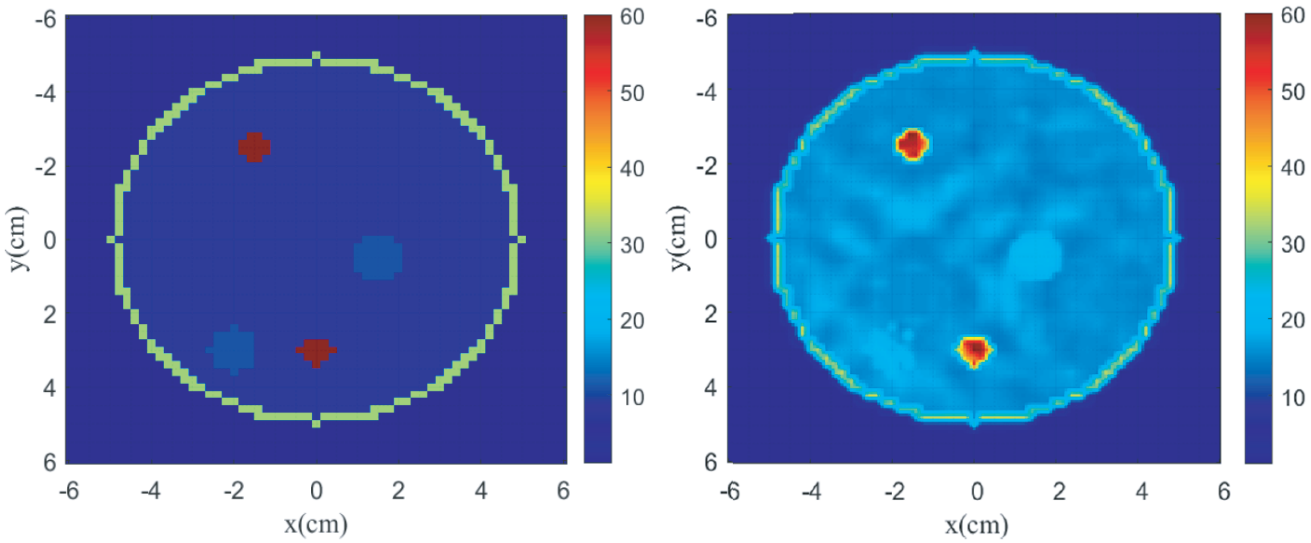

Figure 2. (a) The profile-1 given as input and (b) the output permittivity distribution reconstructed by the proposed method.

Table 2. RMSE error values for profile-1.

Breast tissue type	RMSE
Fatty breast tissue	0.54
Fibro Glandular tissue	0.79
Tumor	0.872

SVBIM has a major role to play in reconstructing higher permittivity values due to the contribution of the variational induced current in every iteration to arrive at a closer estimate of the permittivity profile than BIM or DBIM methods. Additionally, the CS algorithm SpaRSA has the ability to converge to a global minimum. SpaRSA is a greedy CS algorithm that benefits from the use of a good approximate solution as a starting point which helps in reducing the approximation error in each iteration. Hence, SpaRSA and SVBIM together guide the inverse problem to a faster solution even when permittivities to be reconstructed are high.

For a fair comparison, the result produced by the proposed technique is quantitatively compared with other works in literature. For this purpose, the breast profile used by Anjit et al. [3] is adopted in this work (and is given the name Profile-2). In [3], the profile has tumor inclusions with permittivity value of 40 (refer Table 3). This profile-2 is shown in Figures 3(a) and (b).

Table 3. Dielectric constant for tissues in breast profile-2.

Breast profile [30, 31]	Relative permittivity	Conductivity(S/m)
Skin	32	4.0
Fatty breast tissue	9	0.40
Glandular tissue	11	0.45
Tumor	40	4.0

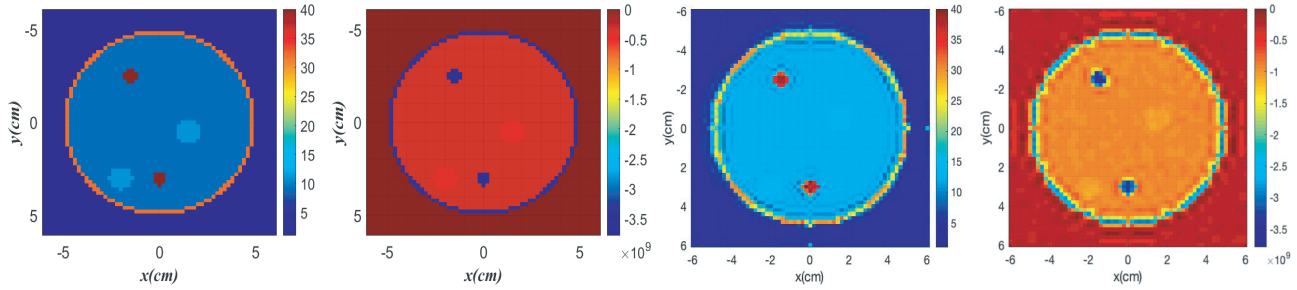

Figure 3. The (a) actual permittivity & (b) actual conductivity of profile-2 and (c) the reconstructed permittivity profile & (d) the reconstructed conductivity profile of profile-2.

Table 4. RMSE value of the reconstructed profiles reconstructed by the proposed method, [3] and [7].

Breast Model	Method	Permittivity, ε_r	RMSE (ε_r)	Conductivity, σ	RMSE (σ)
Tumor	TV [7]	39.15	0.850	3.71	0.290
$\varepsilon = 40$,	RwBP [3]	39.29	0.710	4.31	0.310
$\sigma = 4.0$	Proposed method	39.53	0.470	4.22	0.220
Breast tissue	TV [7]	7.53	1.470	0.318	0.085
12 $\varepsilon = 09$,	RwBP [3]	8.35	0.650	0.427	0.027
$\sigma = 0.40$	Proposed method	8.59	0.410	0.419	0.019
Glandular tissue	TV [7]	09.63	1.370	0.329	0.121
$\varepsilon = 11$,	RwBP [3]	10.31	0.690	0.424	0.026
$\sigma = .45$	Proposed method	10.54	0.460	0.431	0.019

This simulation analysis is performed in the presence of 30 dB noise to model the various types of noise intrusions present in a practical imaging scenario. The reconstructed output for profile-2 is shown in Figures 3(c) and (d). The RMSE error is chosen as the comparison metric in this analysis. Table 4 shows the RMSE values evaluated for the proposed method in comparison to the results reported in [3] and [7]. It can be observed that as compared to both [3] and [7], the permittivity and conductivity values of the various breast tissue types like fatty adipose tissues, fibroglandular tissues, as well as tumor growths have been reproduced with lesser error by the proposed method.

This simulation study suggests that the method proposed in this paper is capable of reconstructing both high and low contrast scenarios. The error levels produced in the reconstruction of the various inclusions is lower than other studies in literature. Therefore, the next step is to experimentally validate these numerical results. The description about the microwave imaging experiment conducted and the corresponding results obtained are discussed in Section 3.2.

3.2. Experimental Validation

The performance of the proposed method is validated against the measurement data from [5]. The imaging experiment described in [5] was performed by the authors' research group. The schematic of the measurement setup is shown in Figure 4.

The aim of the experiment was to image a breast phantom with a cylindrical geometry. The breast phantom was kept inside an anechoic chamber for the imaging process. The phantom was mounted on a turn-table connected to a stepper motor for performing rotation. A standard horn antenna operating in the 2–18 GHz range is used as the source antenna. A receiver antenna with an egg-shaped geometry [5] was used. Imaging was completed by consecutively placing this antenna at angular spacing of 10 degrees,

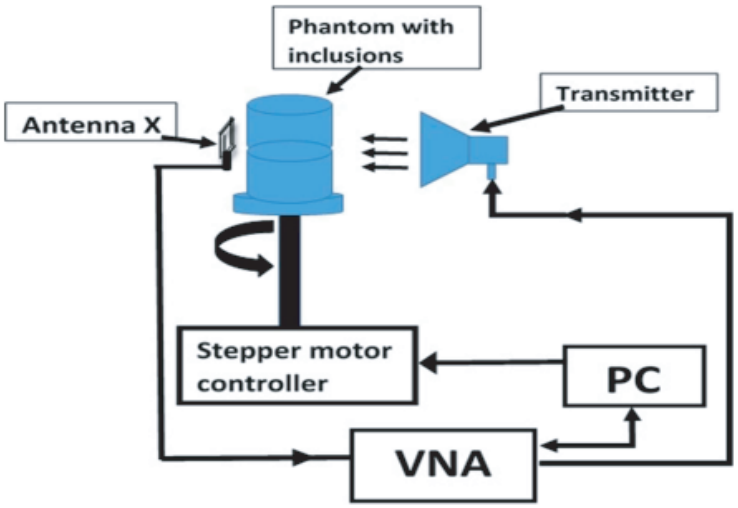

Figure 4. Schematic diagram of the experimental setup.

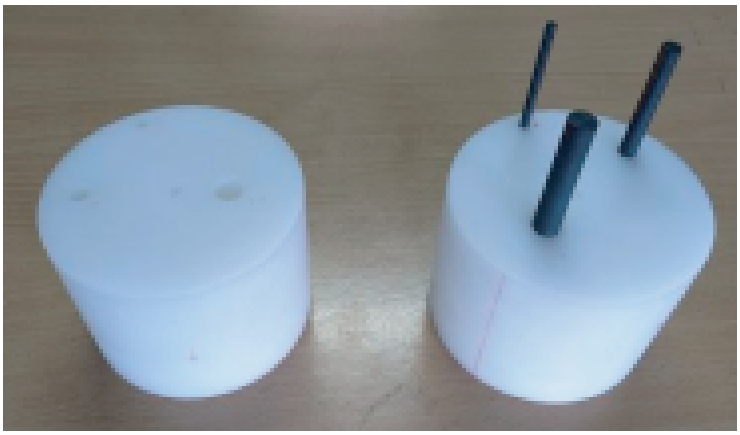

Figure 5. Breast phantom used in the experimental setup.

i.e., at 36 locations around the phantom. PNAE 8362B Agilent network analyser was used to excite the transmitter and also to collect the scattered signals received by the antenna which are then passed on to the personal computer.

The cylindrical breast phantom used in the experiment is shown in Figure 5. This phantom is of diameter 10 cm and height 15 cm. The material selected for the phantom volume is Delrin, (®Dupont) with $\varepsilon_r = 3.7$. This outer region represents the fatty breast tissues. Three inclusions of higher permittivity of ($\varepsilon_r = 4.8$) made of PVC material is used to mimic the tumors. The inclusions are of varying sizes of 10 mm, 6 mm, and 3 mm. This phantom is excited using the horn antenna, and the microwave signals are scattered off it due to the inhomogeneity. The scattered data for 20 frequencies in the 3–4 GHz band is accumulated, and then reconstruction is performed.

In this paper, the SVBIM imaging algorithm in combination with SpaRSA method is used for reconstruction of the experimental data. DBIM along with Tikhonov regularisation was used by Philip et al. in [5], and re-weighted basis pursuit with DBIM was employed by Anjit et al. in [3] to perform reconstruction from the same experimental database. Figure 6(a) shows the cross-section of the breast phantom with three inclusions of sizes 3 mm, 6 mm, and 10 mm. The reconstruction results reported in [3] and [5] are shown in Figures 6(b)–(c). The image reconstructed by the method proposed in this paper is shown in Figure 6(d). It is obtained by accumulating the reconstruction results for 20

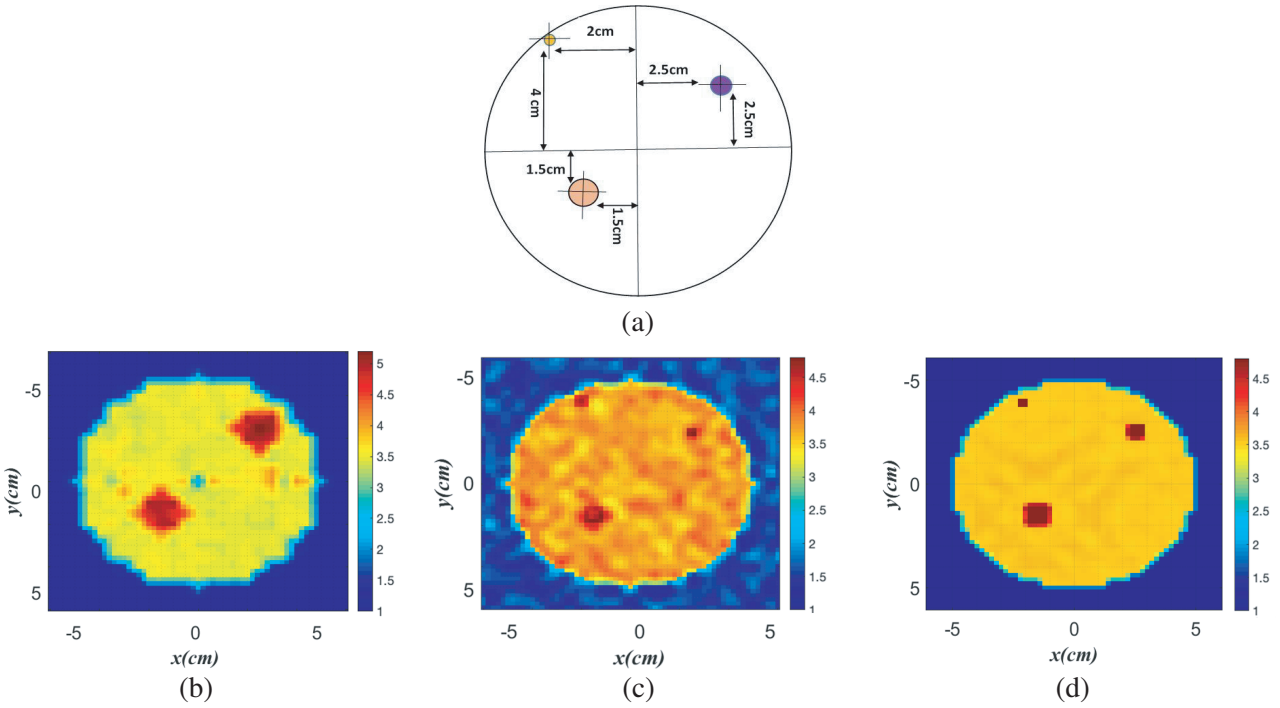

Figure 6. (a) The cross-sectional view of the breast phantom and the reconstructed object profile (b) in [5], (c) in [3] and (d) using the proposed method.

frequencies within the 3–4 GHz band.

Table 5 shows the accuracy in localization and diameter estimation of the inclusions for the proposed method, and it is compared with the results reported in [3] and [5].

Table 5. Comparison of localization and diameter estimation of inclusions produced by the proposed method with [3] and [5].

	Inclusion 1, *diameter* = 10 mm			Inclusion 2, *diameter* = 6 mm			Inclusion 3, *diameter* = 3 mm		
	Location $(-1.5, -1.5)$	Estimated diameter	Error	Location $(2.5, 2.5)$	Estimated diameter	Error	Location $(-2, 4)$	Estimated diameter	Error
Proposed	$(-1.505, -1.505)$	9.11	0.089	$(2.51, 2.50)$	5.2	0.133	$(-2, 4)$	2.2	0.21
Ref. [3]	$(-1.505, -1.515)$	8.32	0.166	$(2.48, 2.50)$	3.8	0.58	$(-1.97, 4.012)$	1.9	0.36
Ref. [5]	$(-1.515, -1.525)$	13.4	0.34	$(2.45, 2.45)$	12.4	1.1	Not detected	Nil	Nil

It may be pointed out that in [5], the reconstruction was performed from the experimental data using DBIM, and only two inclusions could be visualized. On the other hand, in the proposed work and [3], the addition of compressive sensing concepts has helped in the visualization of all the three inclusions. With the help of sparsity, the reconstruction from the same experimental data could be performed as though more experimental data is available. Thus, more information is made available to solve the ill-posed inverse problem, thereby generating the (64×64) reconstructed image shown in Figure 6(d). Compared to [3], the implementation of SVBIM instead of DBIM in this paper has helped to produce an improved localization of all the three inclusions, as can be inferred from Table 5. The diameter of the inclusions estimated by the proposed method is much closer to the actual value producing much smaller error values. The improved tumor localization and size estimation of inclusions as compared to [3] and [5] verifies the efficiency of the proposed method.

4. CONCLUSION

A combinatorial quantitative reconstruction method employing Subspace-based Virtual Born Iteration Method (SVBIM) along with a greedy compressive sensing algorithm, Sparse Reconstruction by Separable Approximation (SpaRSA) to solve the ill-posed inverse problem in microwave imaging is proposed in this paper. Reconstruction of breast profiles with high-permittivity tumor inclusions having permittivity as high as $\varepsilon = 60$ was possible using the proposed method. The above-said imaging technique produces a significantly reduced permittivity error value of 0.47 in the reconstruction of tumor inclusions even in the presence of 30 dB noise as against 0.85 and 0.71 in the case of TV norm and Re-weighted Basis Pursuit methods, respectively. The experimental validation is carried out using a phantom having three inclusions of sizes 10 mm, 6 mm, and 3 mm. The inclusions have been localized successfully with errors of 0.089, 0.133, and 0.21, respectively.

REFERENCES

1. Aldhaeebi, M. A., K. Alzoubi, T. S. Almoneef, S. M. Bamatraf, H. Attia, and O. M. Ramahi, "Review of microwaves techniques for breast cancer detection," *Sensors (Basel)*, Vol. 20, 2390, 2020.
2. Benny, R., T. A. Anjit, and P. Mythili, "An overview of microwave imaging for breast tumor detection," *Progress In Electromagnetics Research B*, Vol. 87, 61–91, 2020.
3. Anjit, T., R. Benny, P. Cherian, and M. Palayyan, "Microwave imaging solutions for medical imaging using re-weighted basic pursuit algorithm," *Progress In Electromagnetics Research M*, Vol. 97, 13–24, 2020.
4. Rocca, P., M. Benedetti, M. Donelli, D. Franceschini, and A. Massa, "Evolutionary optimization as applied to inverse problems," *Inverse Prob.*, Vol. 25, 1–41, 2009.
5. Cherian, P., T. A. Anjit, and P. Mythili, "A compact egg-shaped UWB antenna for breast dielectric profile imaging," *International Journal of Scientific & Technology Research (IJSTR),*, Vol. 9, 2020.
6. Van den Berg, P. M. and A. Abubakar, "Contrast source inversion method: State of art," *Progress In Electromagnetics Research*, Vol. 34, 189–218, 2001.
7. Jamali, N. H., K. A. H. Ping, S. Sahrani, et al., "Image reconstruction based on combination of inverse scattering technique and total variation regularization method," *Indonesian Journal of Electrical Engineering and Computer Science*, Vol. 5, No. 3, 569–576, 2017.
8. Li, J., H. Liu, and Q. Wang, "Enhanced multilevel linear sampling methods for inverse scattering problems," *J. Comput. Phys.*, Vol. 257, Part A, 554–571, 2014.
9. Li, J., P. Li, H. Liu, and X. Liu, "Recovering multiscale buried anomalies in a two-layered medium," *Inverse Problems*, Vol. 31, No. 10, 105006, 28 pages, 2015.
10. Majobi, P. and J. LeVetri, "Comparison of TE and TM inversions in the framework of the Gauss Newton method," *IEEE Trans. Antennas and Propag.*, Vol. 64, 1336–1348, 2010.
11. Shah, P., U. K. Khankhoje, and M. Moghaddam, "Joint L1-L2 regularization for inverse scattering," *2014 IEEE Antennas and Propagation Society International Symposium (APSURSI)*, 868–869, 2014.
12. Candès, E. J. and M. B. Wakin, "An introduction to compressive sampling," *IEEE Signal Processing Magazine*, Vol. 25, 21–30, 2008.
13. Wang, Y., J. Zeng, Z. Peng, X. Chang, and Z. Xu, "Linear convergence of adaptively iterative thresholding algorithms for compressed sensing," *IEEE Transactions on Signal Processing*, Vol. 63, 2957–2971, 2015.
14. Li, R. and S. Osher, "Total variation based image restoration with free local constraints," *International Conf. Image Processing*, Austin, USA, 1994.
15. Poli, L., G. Oliveri, and A. Massa, "Microwave imaging within the first-order Born approximation by means of contrast-field Bayesian compressive sensing," *IEEE Trans. Antennas and Propag.*, Vol. 60, 2865–2879, 2012.

16. Liu, H., M. Petrini, L. Rondi, and J. Xiao, "Stable determination of sound-hard polyhedral scatterers by a minimal number of scattering measurements," *J. Differential Equations*, Vol. 262, No. 3, 1631–1670, 2017.
17. Li, J., H. Liu, and Y. Wang, "Recovering an electromagnetic obstacle by a few phaseless backscattering measurements," *Inverse Problems*, Vol. 33, No. 3, 035011, 20 pages, 2017.
18. Blasten, E. and H. Liu, "Recovering piecewise constant refractive indices by a single far-field pattern," *Inverse Problems*, Vol. 36, No. 8, 085005, 16 pages, 2020.
19. Gao, Y., H. Liu, X. Wang, and K. Zhang, "On an artificial neural network for inverse scattering problems," *J. Comput. Phys.*, Vol. 448, Paper No. 110771, 15 pages, 2022.
20. Yin, W., W. Yang, and H. Liu, "A neural network scheme for recovering scattering obstacles with limited phaseless far-field data," *J. Comput. Phys.*, Vol. 417, 109594, 2020.
21. Jin, K. H., M. T. McCann, E. Froustey, and M. Unser, "Deep convolutional neural network for inverse problems in imaging," *IEEE Transactions on Image Processing*, Vol. 26, 4509–4522, 2017.
22. Anjit, T. A., R. Benny, and P. Mythili, "Non-iterative microwave imaging solutions for inverse problems using deep learning," *Progress In Electromagnetics Research M*, Vol. 102, 53–63, 2021.
23. Benny, R., T. A. Anjit, and P. Mythili, "Deep learning based non-iterative solution to the inverse problem in microwave imaging," *Progress In Electromagnetics Research M*, Vol. 109, 231–240, 2022.
24. Wei, Z. and X. Chen, "Deep-learning schemes for full-wave nonlinear inverse scattering problems," *IEEE Trans. Geosci. Remote Sens.*, Vol. 57, 1849–1860, 2019.
25. Zhang, L., K. Xu, R. Song, et al., "Learning-based quantitative microwave imaging with a hybrid input scheme," *IEEE Sensors Journal*, Vol. 20, 15007–15013, 2020.
26. Cheng, Y. and M. Fu, "Dielectric properties for non-invasive detection of normal, benign, and malignant breast tissues using microwave theories," *Thoracic Cancer*, Vol. 9, 459–465, 2018.
27. Liu, Z. and Z. Nie, "Subspace-based variational born iterative method for solving inverse scattering problems," *IEEE Geoscience and Remote Sensing Letters*, Vol. 16, 1017–1020, 2019.
28. Wright, S. J., R. D. Nowak, and M. A. T. Figueiredo, "Sparse reconstruction by separable approximation," *IEEE Transactions on Signal Processing*, Vol. 57, 2479–2493, 2009.
29. Shi, X., H. Wang, and S. H. Leung, "Iterative sparse channel estimator based on SpaRSA approach," *International Conference on Computer Science and Network Technology (ICCSNT), Dalian, China*, 356–360, 2017.
30. Tavassolian, N., H. Kanj, and M. Popovic, "Assessment of dark eyes antenna radiation in the vicinity of the realistic breast model," *12th International Symposium on Antenna Technology and Applied Electromagnetics (ANTEM)*, Montreal, Canada, July 2006.
31. Fear, E. C. and M. Okoniewski, "Confocal Microwave Imaging for breast tumor detection: Application to a hemispherical breast model," *2002 IEEE MTT-S International Microwave Symposium Digest*, Vol. 3, 1759–1762, 2002.